JOURNAL OF GEOPHYSICAL RESEARCH, VOL. ???, XXXX, DOI:10.1029/,

Supplementary Material: Layered crustal anisotropy around the San Andreas Fault near Parkfield, California

Pascal Audet

Department of Earth Sciences, University of Ottawa, Canada

1. Receiver functions from PASO stations

Figures (S1)-(S3) show binned receiver functions and harmonic decomposition for three representative stations that are part of the temporary PASO network: PIES, CGAS, and GLEN, respectively. These results show the high quality of the recovered receiver function bins and of their corresponding harmonic components, despite the short duration of the experiment and the lower number of high-SNR P-wave seismograms.

2. Effect of modal decomposition

Numerous receiver function studies deconvolve the vertical (Z) component from the radial (R) and transverse (T) components. Due to the incomplete isolation of the P wave on the Z component, the deconvolution procedure generates a positive arrival at zero-lag on the R-component receiver function, whereas the T component should be minimally affected. In this paper we further decompose the Z-R-T components into the compressional (P), shear radial (S_V) and shear transverse (S_H) components of motion (i.e., modal decomposition). This decomposition is weakly sensitive to the near-surface

---

velocities, and better isolates the P wavelet onto a single component of motion, thereby avoiding the zero-lag signal on the S_V-component receiver function. The S_H-component receiver function is again only weakly affected by this procedure.

Figure (S4) shows the receiver functions for station PKD using both the Z-R-T system and the P-S_V-S_H decomposition. The receiver functions are for the most part identical except around the zero-lag time, where a large signal is observed on the radial-component receiver functions from the Z-R-T system. The modal decomposition may therefore be better suited to resolve very near-surface structure that would otherwise be blurred on the radial component calculated in the Z-R-T system.

3. Dipping interface and zero-lag amplitudes

The effect of a dipping interface can generally be observed as back-azimuthal variations of the zero-lag amplitude on the tangential (transverse) component [**?**]. This is due to the amplitude of the direct P wave having an azimuthal dependence. Figures (S5) and (S6) show the variations of the zero-lag amplitude as a function of back-azimuth for both the Z-R-T and the P-S_V-S_H receiver functions. The amplitudes do not display a clear $1-\theta$ periodicity pattern that would indicate the effect of dipping structures. We therefore interpret the various harmonic components as a reflection of layered seismic anisotropy.

4. Inversion results

Figures (S7) and (S8) show results of the inversion for the upper and bi-layered anisotropy models, respectively. See main (sections 4.1.1 and 4.1.2) text for details.

5. Harmonic decomposition of synthetic data

The harmonic decomposition of receiver functions is useful in the visualization of anisotropic signals; however their interpretation is non-unique. In particular it is difficult to separate the effects of dipping interfaces from those of elastic anisotropy. In this section we generate sets of receiver functions using a the approach developed by **?** for three reference models. In each case only the geometry of the model is relevant - we discard the amplitude information and plot the total variance over the model depth range in order to examine the behavior of the harmonic terms as we vary structural parameters. The harmonic components are also rotated to the natural geometry of the model, and the B and C terms correspond to the $B_\perp$ and $C_\perp$ terms, respectively.

The first model is characterized by a dipping Moho, where dip is varied between 0 to 50 degrees (Fig. S9a). For a flat Moho the variance is maximum on the A term and zero for the higher harmonics. As dip increases, the B term (1-θ harmonic) increases rapidly and becomes the dominant term for dip larger than 20 degrees. The C term slowly increases with increasing dip, whereas the A term decreases steadily. The slight increase of the C term variance is likely due to the mis-migration of wave conversions that leaks information into higher degrees. The flattening of both A and C terms beyond a dip of 40 degrees is an artifact of the waveform modeling technique [**?**].

The second and third models are characterized by a mid crustal anisotropic layer, with or without a Moho discontinuity. The anisotropy is characterized either by a slow or fast axis of hexagonal symmetry, and the variance of each term is plotted as a function of the plunge of the symmetry axis (Fig. S9b,c). The most salient feature in these plots is the change in the A term betwen the two models, showing the effect of the Moho discontinuity.

Interestingly the difference between the two cases (fast vs. slow axis) is only visible in the A term for the model with a Moho discontinuity; in all other cases the model of hexagonal symmetry is undistinguishable. We note, however, that only the variance is plotted here, and these models can in fact be distinguished by considering the sign of the wave conversions as well as the recovered azimuth α_C. In all cases we note that the B term is maximum for a plunge of 40-50 degrees, depending on the model of hexagonal symmetry. Although they provide purely qualitative information, these tests are useful to discriminate between end-member models.

Table S1. Stations used in this study, along with the number of successful receiver functions (# teleseismic events with SNR>7.5) and the number of independent back-azimuth/slowness bins used in the harmonic decomposition. High quality data from the permanent stations SAO and PKD yielded almost 2 orders of magnitude more receiver functions from 12 years of data compared to stations of the PASO network that only operated for just over a year (June/July 2001 to October 2002).

Station (network)	Latitude	Longitude	# teleseismic events	# bins
PKD (BK)	35.945	-120.542	1342	159
SAO (BK)	36.764	-121.447	1580	167
AHAB (XN)	35.9767	-120.5445	37	20
ALEX (XN)	35.9788	-120.4647	27	16
BECH (XN)	35.9509	-120.5475	39	22
BUZZ (XN)	36.0166	-120.6049	41	24
CGAS (XN)	35.9691	-120.5000	32	25
CRAB (XN)	36.0117	-120.5535	50	28
CRAK (XN)	35.9555	-120.5225	40	25
CVCR (XN)	35.9948	-120.5280	42	24
DBLT (XN)	35.9602	-120.5844	49	26
FLIP (XN)	35.9715	-120.5329	30	20
GLEN (XN)	35.9335	-120.5645	53	35
GOBI (XN)	35.9399	-120.5425	48	29
GULY (XN)	35.9492	-120.5115	32	19
HIDE (XN)	35.9660	-120.5488	42	27
KOOL (XN)	36.0032	-120.5469	39	18
LEEP (XN)	35.9929	-120.5066	54	31
MOH9 (XN)	35.9737	-120.5673	58	31
MRED (XN)	35.9638	-120.4835	42	23
NOXV (XN)	35.9576	-120.5614	37	22
PAKD (XN)	35.9820	-120.5617	36	21
PIES (XN)	35.9970	-120.5577	36	23
PIGH (XN)	35.9633	-120.5663	38	22
POLE (XN)	36.0055	-120.5744	44	26
POND (XN)	36.0148	-120.5707	39	23
POST (XN)	36.0284	-120.5725	20	12
POWR (XN)	36.0077	-120.5342	49	28
PRIS (XN)	35.9782	-120.4893	43	22
RAIN (XN)	35.9842	-120.4857	39	21
RCKY (XN)	35.9613	-120.6052	56	30
STGI (XN)	36.0264	-120.5882	37	21
VINE (XN)	35.9462	-120.5391	36	24

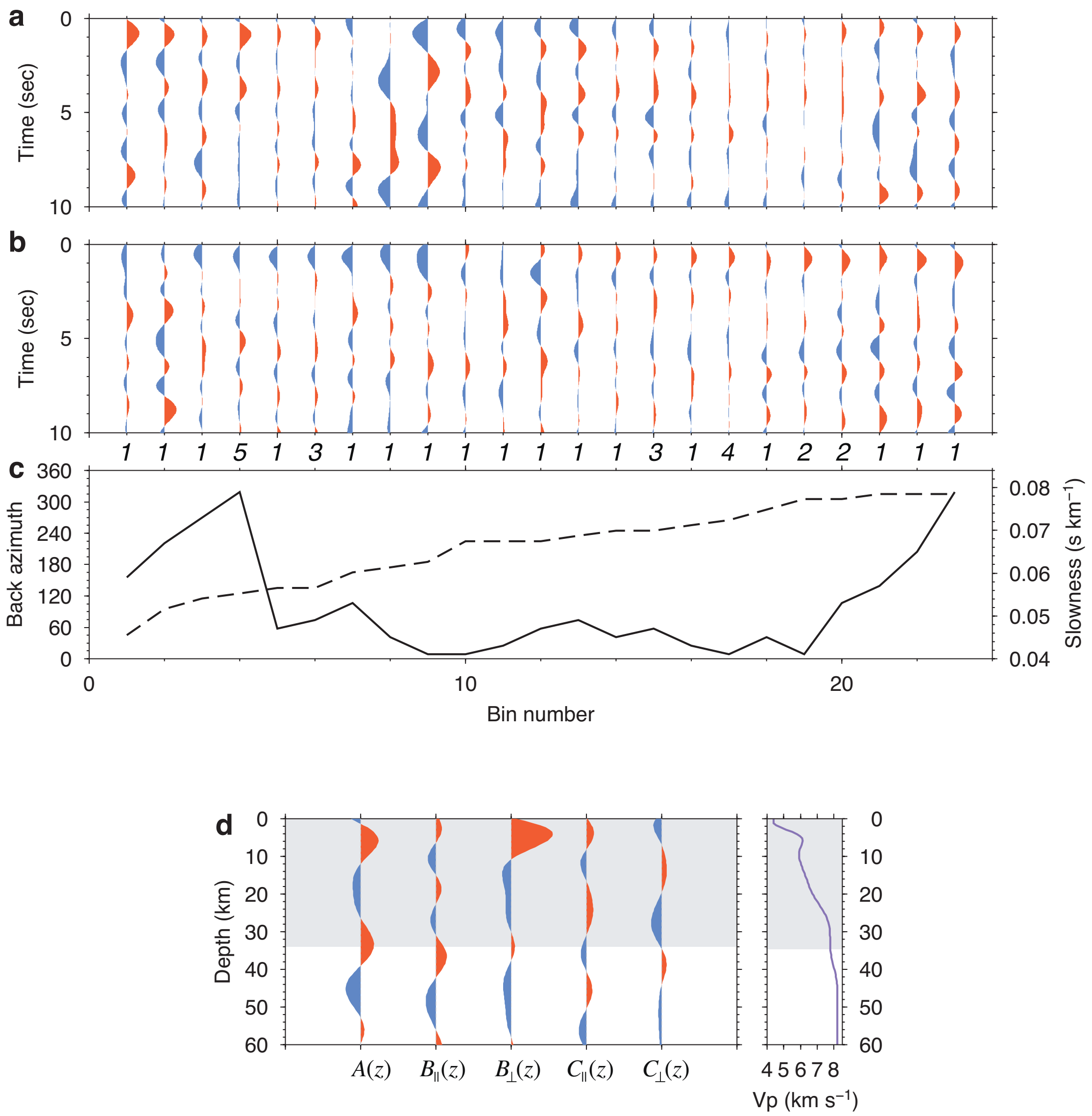

Figure S1. Radial (a) and transverse (b) component receiver function data for station PIES. Figure format for (a-c) is the same as Figure 2. Numbers between panels (b) and (c) indicate the number of receiver functions per bin. Panel (d) shows the harmonic decomposition of both radial and transverse components.

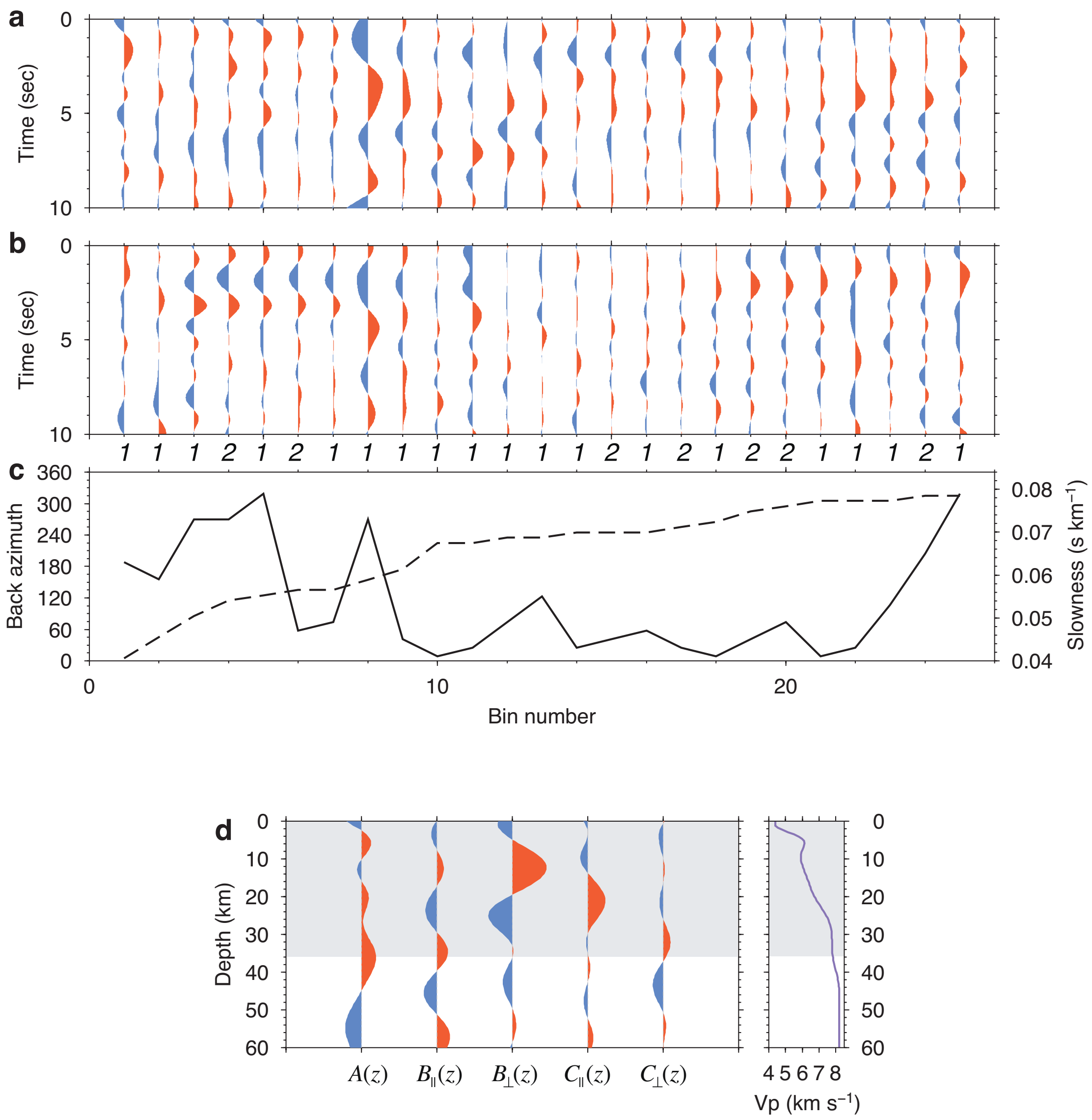

Figure S2. Radial (a) and transverse (b) component receiver function data for station CGAS. Figure format for (a-c) is the same as Figure 2.

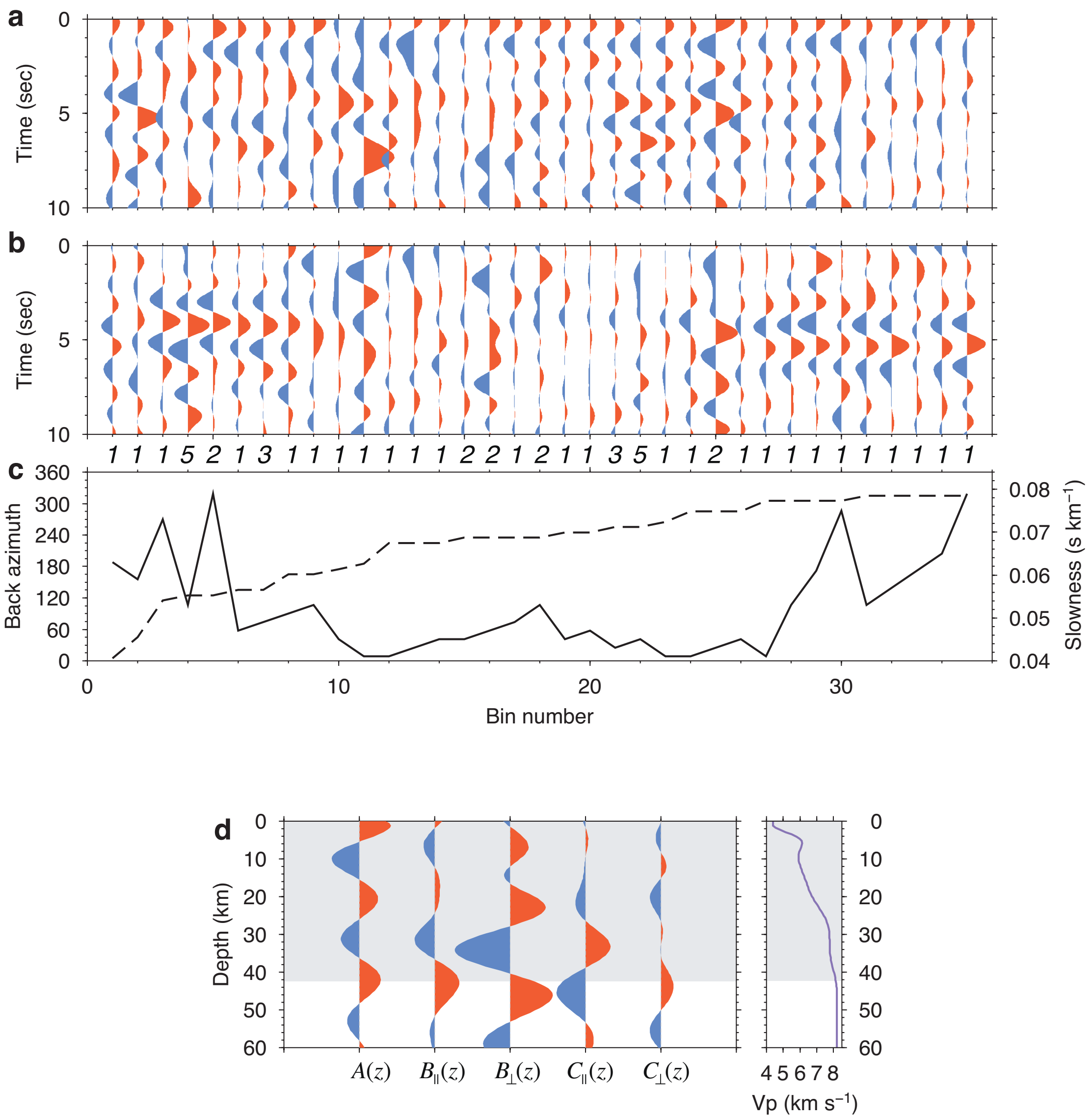

Figure S3. Radial (a) and transverse (b) component receiver function data for station GLEN. Figure format for (a-c) is the same as Figure 2.

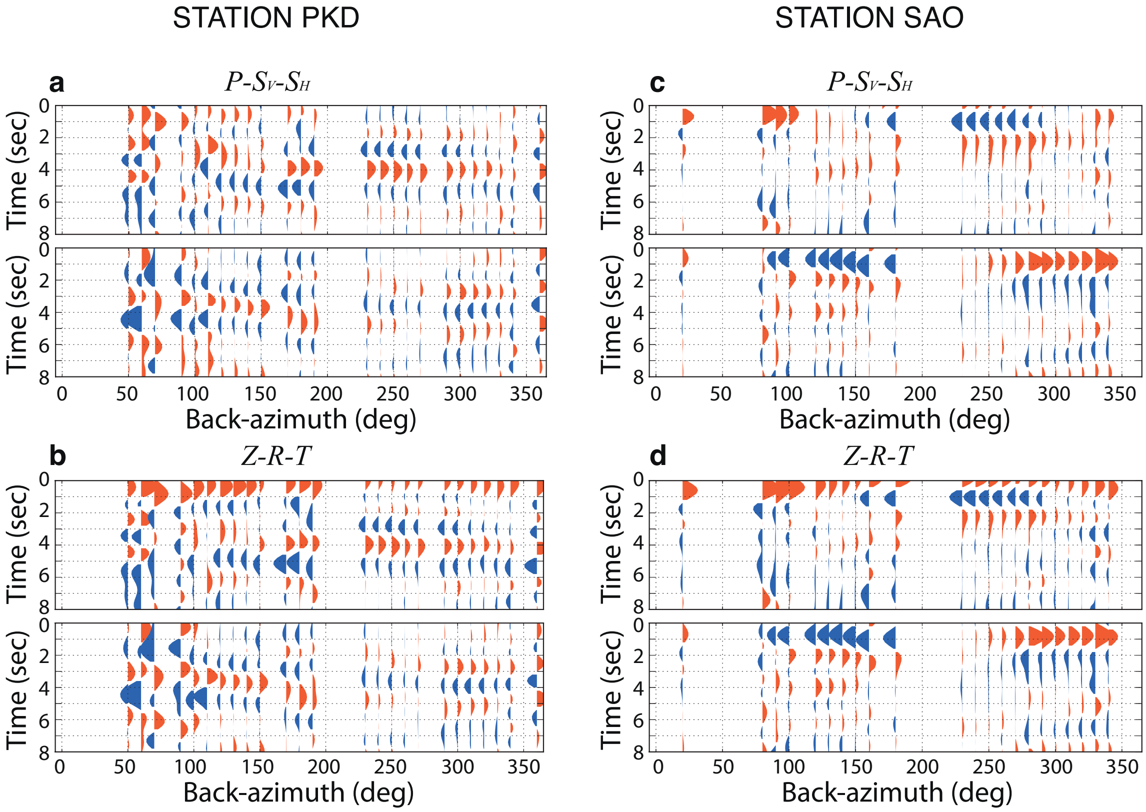

Figure S4. Receiver functions for stations PKD (a,b) and SAO (c,d) obtained from the modal decomposition (a,c) and standard Z-R-T system, for both radial (top panels) and transverse (bottom panels) components. Receiver functions are ordered by back-azimuth of incoming wavefield. This figure shows that the receiver functions are equivalent, except near the zero-lag time for radial components, where the modal decomposition does not produce a large positive pulse.

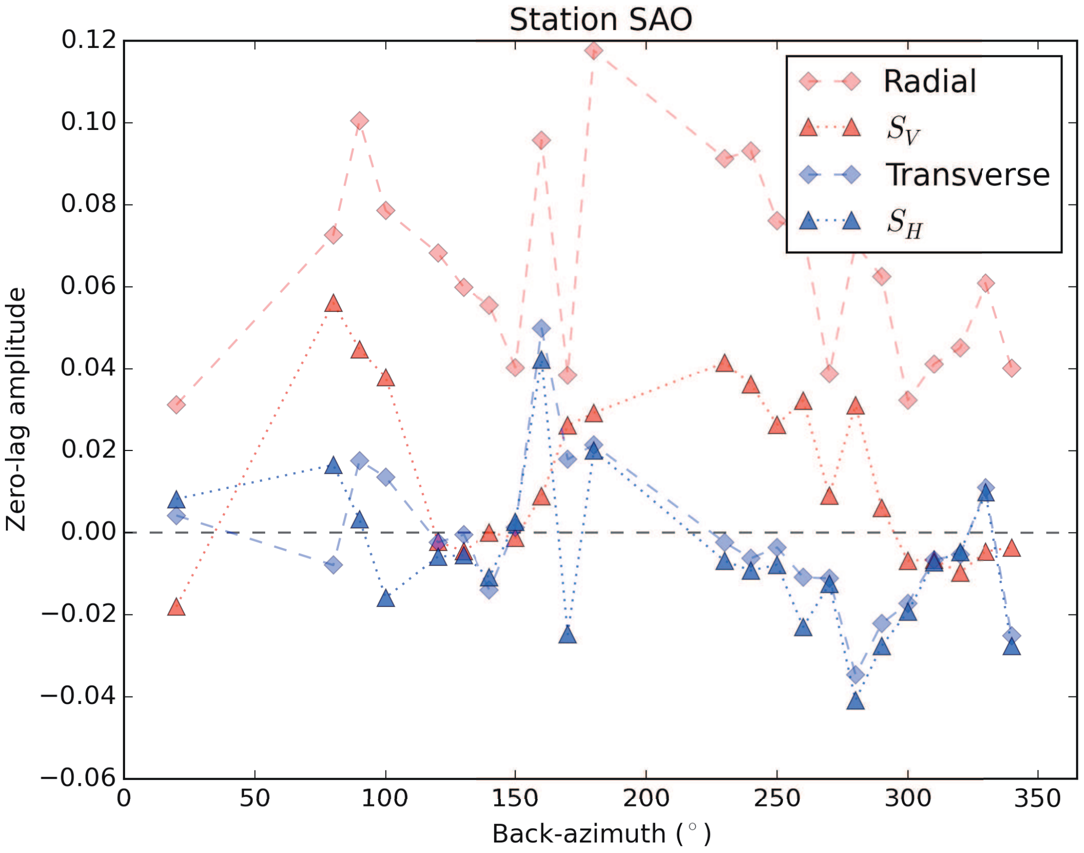

Figure S5. Zero-lag amplitude variations for station SAO for the radial (red) and transverse (blue) components obtained from the *Z*-*R*-*T* (faint colors and dashed lines) and the P-S_V-S_H system (bright colors and dotted lines). This figure shows how the radial component is affected by the zero-lag pulse, whereas the transverse components are sensibly equivalent.

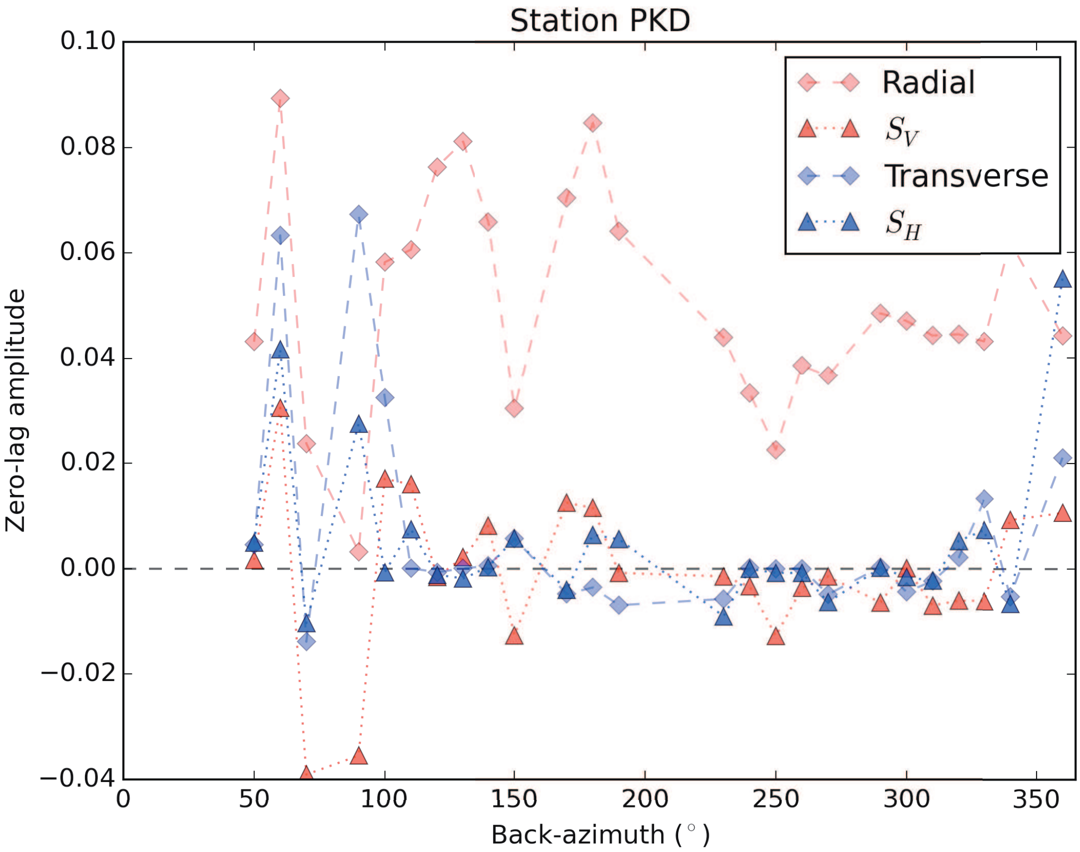

Figure S6. Zero-lag amplitude variations for station PKD. Figure format is the same as Figure (S5)

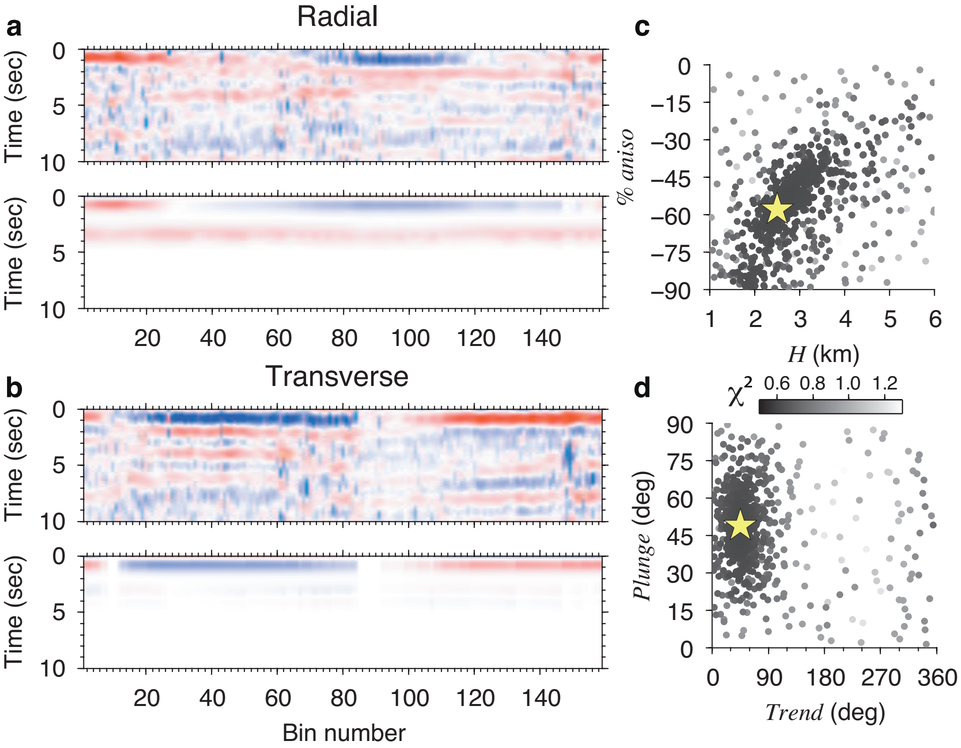

Figure S7. Results of the Monte Carlo inversion of receiver functions at station SAO for parameters of the upper crustal anisotropic layer. Panels (a,b) show the observed (top) and best-fit synthetic (bottom) receiver functions for both radial (a) and transverse (b) components. Panels (c,d) show the misfit value through 2D slices of the parameter space. The yellow stars indicate parameters of the best-fit model.

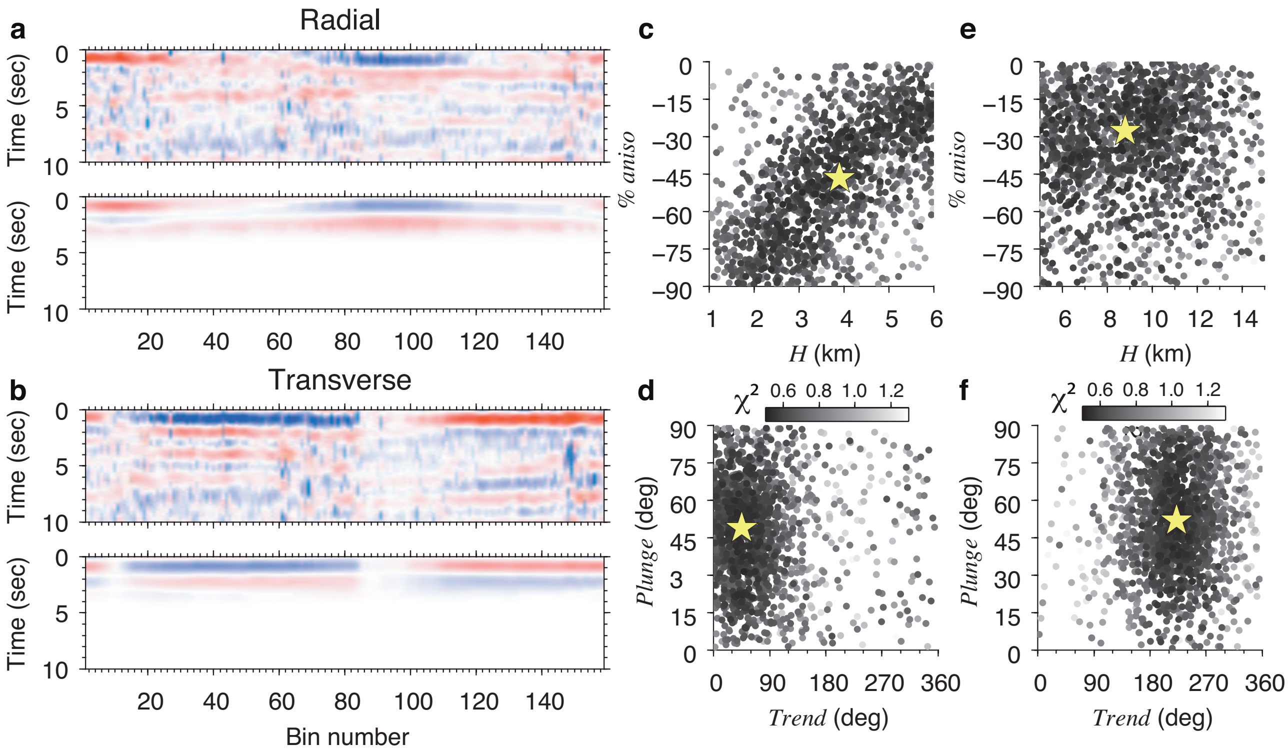

Figure S8. Results of the Monte Carlo inversion of receiver functions at station SAO for parameters of the upper and mid crustal anisotropic layers. Figure format is the same as Figure (S7). Panels (c,d) and (e,f) show the misfit values corresponding to the upper and mid crustal layers, respectively. The yellow stars indicate parameters of the best-fit model.

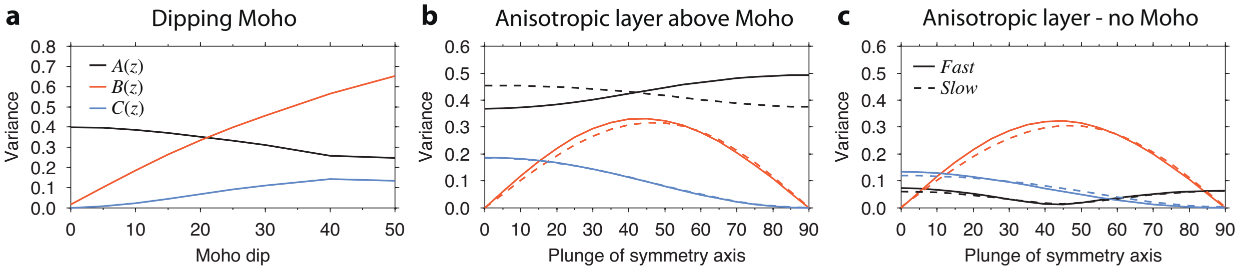

Figure S9. Harmonic decomposition of synthetic receiver functions for three different cases: a) an isotropic velocity model with a dipping crust-mantle interface; b) a 7 km thick anisotropic lower-crust placed immediately above the Moho; and c) a 7 km thick anisotropic layer embedded within an isotropic crustal half-space. Curves represent the variance of each harmonic component with black, red and blue curves corresponding to the constant term (A), the first harmonic ($B_\perp$) and the second harmonic ($C_\perp$).